

SMOS Near-Real-Time Soil Moisture processor. Part 1: Neural network evaluation and algorithm description

ESA contract 4000101703/10/NL/FF/fk CCN4
Technical Officer: M. Drusch

CESBIO-SMOS report **SO-TN-CB-GS-0049 v1.5**

N.J. Rodríguez-Fernández¹, P. Richaume¹, J. Muñoz-Sabater²,
P. de Rosnay², Y.H. Kerr¹

¹ **CESBIO**

UMR 5126 (CNRS, CNES, UPS, IRD),
18 av. Edouard Belin, bpi 2801, 31401 Toulouse cedex 9, France

² **ECMWF**

Shinfield Park, Reading, RG2 9AX, UK

Dec 1st, 2015



Revision history

| Date | Rev | Description | Author |
|-------------|------|--|--------|
| 16/Dec/2014 | v1.1 | First draft | NRF |
| 14/Jan/2015 | v1.2 | Including comments from PdR | NRF |
| 20/Apr/2015 | v1.3 | Analysis of best strategy to compute I_2 | NRF |
| | | Including NN specifications | NRF |
| | | Validation against ISMN data | NRF |
| 15/Jul/2015 | V1.4 | Including temporal correlation maps and monthly averages for the proposed NRT NN configuration | NRF |
| 5/Oct/2015 | V1.5 | Including error computation | NRF |
| 1/Dec/2015 | | Updated flow chart | NRF |

Contents

| | | |
|----------|--|-----------|
| 1 | Introduction | 5 |
| 2 | Best configuration for a NRT SM processor | 6 |
| 2.1 | Input data | 6 |
| 2.2 | Sensitivity to the probability of RFI | 8 |
| 2.3 | Computation of T_b 's and SM local extremes tables | 10 |
| 2.4 | Number of neurons | 11 |
| 3 | Evaluation of the recommended NN configuration for the NRT SM processor | 14 |
| 3.1 | Comparison to SMOS L3 SM | 14 |
| 3.2 | Comparison to in situ measurements | 15 |
| 4 | The NRT SM processor implementation | 17 |
| 4.1 | Global architecture | 17 |
| 4.2 | NRT SM algorithm | 18 |
| 4.2.1 | Neural network output uncertainties | 20 |
| 5 | Summary | 23 |

Abstract

The best approach to retrieve soil moisture in Near-Real-Time (NRT) using neural networks (NNs) has been discussed using SMOS CATDS Level 3 brightness temperatures and Level 3 soil moisture (SM). NN retrievals have been first evaluated comparing the output SM to the L3 SM. The NN output has also been evaluated against in situ measurements over the SCAN network, the USDA ARS watersheds and OzNet. The recommended input configuration for the NRT SM processor is using SMOS T_b 's from 30° to 45° incidence angles in 5° bins for both H and V polarizations, and a corresponding set of normalized indexes computed taking into account the brightness temperatures local extreme values and the associated L3 SM values. Finally, the input data should add the 0-7 cm soil temperature forecast by ECMWF. The recommended NN architecture is two layers with a hidden layer containing 5 non-linear neurons and an output layer with one linear neuron. This configuration is the best trade-off of retrieval performance and swath width (914 km). The recommended NN configuration for the NRT SM product has been specifically evaluated against the reference L3 SM data and against a large number of in situ measurements from the International Soil Moisture Network. Average statistics are somewhat better than those of the reference L3 SM data for most of the sites. In summary, the recommended NN configuration performs as well or better than the reference SM dataset but the retrieval can be done in Near-Real-Time after a global training phase. Finally, the recommended processor architecture is discussed.

1 Introduction

The objective of this document is to define the best neural network (NN) configuration to implement a Near-Real-Time (NRT) soil moisture (SM) processor from SMOS observations. This work follows that of the SMOS+NN project (Rodríguez-Fernández et al., 2013, 2014, 2015), whose objectives were to do a feasibility study of the use of neural networks to retrieve SM from SMOS observations.

The NRT SM product should be as similar as possible to the operational L2 SM product and it should be provided in the same grid (ISEA grid common to L1 and L2 ESA products). A NRT processor needs to find a trade-off in between the best retrieval quality and the larger swath-width. Therefore, the work done during the SMOS+NN project has been extended using different combinations of incidence angle ranges from 1 (40-45 deg) to 7. The exact angle range for each model configuration and the associated swath half-width is given in Table 1. Using SMOS brightness temperatures (T_b 's) only in the 40°-45° incidence range allows SM retrievals in the full swath (2×588 km). Increasing the number of angle bins decreases the width of the swath where SM can be retrieved. For instance, the swath width will be 2×457 km or 2×334 km when using angles in the 30-45° or in the 25-60° range, respectively. Figure 1 shows a comparison of those three swath widths over Africa and Western Europe.

The SMOS+NN (Rodríguez-Fernández et al., 2013) database has been used to train NNs using SMOS T_b 's, MODIS NDVI, ECMWF soil temperature and ECOCLIMAP soil texture as input. Taking into account the constrains of a NRT SM product (Sect. 1), the SMOS L3 SM has been used as reference for the supervised learning phase. Both Level 3 SM and T_b 's are CATDS data version RE01.

The evaluation strategy of Rodríguez-Fernández et al. (2013) has been adopted. The NN has been trained using data of 2012, taking one day every five and one grid point over two both in longitude and latitude. A validation data set is selected randomly within this dataset and containing 20 % of the data. The performance of the NN is checked for all iterations during the training phase to detect possible signs of over-learning. No over-learning has been detected for any of the NN trained. A subset of 60 % of the data is used for the actual training and determination of the NN weights. After training the NN, the correlation, RMSE and mean absolute error (MAE) with respect to SMOS L3 SM has been evaluated with the final 20 % of the data set. The results are listed in columns 2 to 4 of Table 2.

In addition, the NN results have been evaluated against in situ measurements of the USDA SCAN networks (Schaefer et al., 2007), the USDA watersheds networks in the USA (Jackson et al., 2012) and representative stations of the Australian OzNet network (Smith et al., 2012). The mean STD, R and bias for each NN configuration with respect to the *in situ* measurements are listed in columns 5-7 of Table 2. For comparison purposes, the ECMWF IFS (Integrated Forecasting System) operational top layer (0-7cm) soil moisture and the SMOS L3 SM evaluation against in situ measurements is shown in Table 1.

Finally, for some of the NN configurations, three years of SMOS data from 1/6/2010 to 23/6/2013 have been retrieved and the correlation of the NN SM and the SMOS L3 SM have been evaluated as follows (see Rodríguez-Fernández et al., 2015). For each day, the daily or spatial correlation R_{spa} has been evaluated. From the time series of R_{spa} , it has been computed the mean value. These values are given in column 8 of Table 2. On the other hand, the temporal correlation R_{temp} between NN SM and SMOS L3 SM has been computed for each grid point for the 3-year period. From the maps of R_{temp} it has been computed the mean value (column 9 of Table 2). Some maps are shown in Fig. 2.

The rest of this document is organized as follows: Section 2 discusses different NN configurations using SMOS L3 SM data as reference for the training and taking into account the constrains of a NRT system. Section 3 presents an evaluation of the performances of the proposed NN configuration for the NRT SM product against SMOS L3 SM and *in situ* measurements of SM. Finally, Section 4 discusses the proposed NRT SM processor architecture and flow chart as well as the specifications of the neural network itself .

Table 1: Evaluation of ECMWF surface SM and SMOS L3 SM against in situ measurements (for the same period as those in Table 2). The results are presented as a function of the incidence angle range measured by SMOS (second column), which determines the swath width (third column). Columns 4-6 show the mean standard deviation, correlation and bias of different SM products with respect to the *in situ* validation sites. Note that the quality of the operational SMOS L3 SM product increases significantly as the number of incidence angles accessible to SMOS increases.

| | Angle range (deg) | Swath width (km) | Mean STD | Mean R | Mean Bias |
|---------|-------------------------|------------------------|-------------|-----------|--------------|
| ECMWF | ... | ... | 0.049 | 0.59 | 0.056 |
| SMOS L3 | 40-45 | 1176 | 0.063 | 0.46 | -0.019 |
| SMOS L3 | 35-45 | 1078 | 0.062 | 0.48 | -0.016 |
| SMOS L3 | 30-45 | 914 | 0.064 | 0.50 | -0.026 |
| SMOS L3 | 25-45 | 758 | 0.061 | 0.52 | -0.022 |
| SMOS L3 | 25-60 | 668 | 0.058 | 0.53 | -0.023 |

2 Best configuration for a NRT SM processor

2.1 Input data

Table 2 gives the results for NNs that use different datasets as input including SMOS information for different incident angle bins, NDVI, soil temperature and texture. The SMOS observables are T_b 's but in addition a local normalization of the T_b 's (index I_1 of Rodríguez-Fernández et al., 2013) and a local normalization of the T_b 's scaled to the minimum and maximum local SM values (index I_2 of Rodríguez-Fernández et al., 2013) have also been studied.

It is possible to pre-process SMOS T_b 's to compute a local index (hereafter index I_1) by normalizing from 0 to 1 the brightness temperature for each polarization and incidence angle. First, the maximum (T_b^{max}) and minimum (T_b^{min}) of the T_b 's in the time series for a given latitude (λ) and longitude (ϕ) grid point and for each polarization and incidence angle bin. The local normalized index can be computed as:

$$I_{2\lambda\phi}(t) = SM_{\lambda\phi}^{T_b^{min}} + [SM_{\lambda\phi}^{T_b^{max}} - SM_{\lambda\phi}^{T_b^{min}}]I_{1\lambda\phi}(t) \quad (1)$$

Where

$$I_{1\lambda\phi}(t) = \frac{T_{m\lambda\phi}(t)}{T_{D\lambda\phi}} \quad (2)$$

With $T_{m\lambda\phi}(t) = T_{b\lambda\phi}(t) - T_{b\lambda\phi}^{min}$ and $T_{D\lambda\phi} = T_{b\lambda\phi}^{max} - T_{b\lambda\phi}^{min}$. As I_1 , the index I_2 is computed for each incidence angle bin and polarization at the time t of the SMOS acquisition. The information content of index I_2 is very strong as it contains a local information on the dynamic ranges of both the measured T_b 's and the model SM.

When using only T_b 's as SMOS information, even adding additional input data, one should definitely use as many incidence angles as possible as all the quality metrics improve. In contrast, using index I_2 , it is possible to obtain good results with less than 7 incidence angles and using less complementary data as input. **The best compromise is using three incidence angles as input (both for H and V polarizations) and soil temperature (NN [I_2 & $T_b(30^\circ-45^\circ)$, T]) as the quality metrics are within 3 % of those of NN retrievals using 7 incidence angles but the swath width is 250 km larger (up to 914 km).** Using less incidence angles makes the quality metrics to decrease by 5-10 % and would require to use also NDVI as input to improve the results, which will introduce significant constrains in a NRT operational processor as MODIS data will also be needed.

Table 2: Global evaluation in 2012 with respect to SMOS L3 SM (columns 2 to 4, correlation, RMSE and Mean Absolute Error), statistics with respect to *in situ* measurements (columns 5 to 7, STD, R and Bias are the standard deviation of the differences time series, the Pearson correlation coefficients and the bias (mean of NN SM minus de mean of *in situ* SM) averaged across all the *in situ* sites). Finally the spatial and temporal correlation of 3 years times series with respect to SMOS L3 SM are given in columns 8 and 9. Some of the input configuration includes MODIS NDVI (“VI”), sand and clay fractions (“tex”) and soil temperature in the 0-7 cm layer from ECMWF IFS (“T”).

| input | R | RMSE | MAE | STD | R | Bias | Mean R_{spa} | Mean R_{temp} |
|--|-------------|--------------|--------------|--------------|-------------|---------------|----------------|-----------------|
| Using only Tb's | | | | | | | | |
| $T_b(H,V,30^\circ-45^\circ),T$ | 0.81 | 0.065 | 0.041 | 0.052 | 0.50 | -0.028 | 0.77 | 0.70 |
| $T_b(H,V,30^\circ-45^\circ),tex,VI$ | 0.78 | 0.068 | 0.044 | 0.046 | 0.54 | -0.025 | | |
| $T_b(H,V,30^\circ-45^\circ),T,VI$ | 0.81 | 0.063 | 0.040 | 0.048 | 0.51 | -0.027 | | |
| $T_b(H,V,30^\circ-45^\circ),T,tex$ | 0.82 | 0.063 | 0.039 | 0.052 | 0.50 | -0.025 | 0.78 | 0.70 |
| $T_b(H,V,30^\circ-45^\circ),tex,VI,T$ | 0.83 | 0.061 | 0.038 | 0.049 | 0.51 | -0.026 | 0.81 | 0.76 |
| $T_b(H,V,25^\circ-60^\circ),VI,T$ | 0.85 | 0.052 | 0.032 | 0.051 | 0.57 | -0.031 | | |
| $T_b(H,V,25^\circ-60^\circ),T,tex$ | 0.86 | 0.051 | 0.031 | 0.050 | 0.56 | -0.028 | 0.82 | 0.79 |
| $T_b(H,V,25^\circ-60^\circ),VI,T,tex$ | 0.86 | 0.051 | 0.031 | 0.050 | 0.57 | -0.026 | 0.82 | 0.78 |
| Using local normalization of T_b's (I_1) | | | | | | | | |
| $I_1 \& T_b(H,V,30^\circ-45^\circ),T$ | 0.81 | 0.064 | 0.041 | 0.054 | 0.52 | -0.028 | 0.77 | 0.73 |
| $I_1 \& T_b(H,V,30^\circ-45^\circ),T,tex$ | 0.83 | 0.061 | 0.039 | 0.054 | 0.51 | -0.027 | 0.78 | 0.74 |
| $I_1 \& T_b(H,V,30^\circ-45^\circ),VI$ | 0.78 | 0.068 | 0.045 | 0.051 | 0.54 | -0.026 | | |
| $I_1 \& T_b(H,V,30^\circ-45^\circ),VI,T$ | 0.82 | 0.062 | 0.039 | 0.050 | 0.53 | -0.030 | 0.79 | 0.77 |
| $I_1 \& T_b(H,V,30^\circ-45^\circ),VI,tex$ | 0.79 | 0.067 | 0.044 | 0.050 | 0.56 | -0.027 | | |
| $I_1 \& T_b(H,V,30^\circ-45^\circ),VI,T,tex$ | 0.83 | 0.061 | 0.038 | 0.051 | 0.53 | -0.026 | | |
| $I_1 \& T_b(H,V,25^\circ-45^\circ),T$ | 0.83 | 0.060 | 0.037 | 0.054 | 0.53 | -0.030 | | |
| $I_1 \& T_b(H,V,25^\circ-45^\circ),VI$ | 0.79 | 0.066 | 0.043 | 0.052 | 0.57 | -0.029 | | |
| $I_1 \& T_b(H,V,25^\circ-45^\circ),VI,T$ | 0.83 | 0.059 | 0.037 | 0.052 | 0.55 | -0.030 | | |
| $I_1 \& T_b(H,V,25^\circ-60^\circ),T$ | 0.85 | 0.051 | 0.032 | 0.050 | 0.56 | -0.030 | 0.82 | 0.79 |
| $I_1 \& T_b(H,V,25^\circ-60^\circ),VI$ | 0.81 | 0.058 | 0.037 | 0.049 | 0.58 | -0.030 | | |
| $I_1 \& T_b(H,V,25^\circ-60^\circ),VI,T$ | 0.86 | 0.051 | 0.031 | 0.052 | 0.57 | -0.029 | 0.82 | 0.79 |
| Using local normalization of T_b's with SM extreme values (I_2) | | | | | | | | |
| $I_2 \& T_b(H,V,40^\circ-45^\circ)$ | 0.83 | 0.060 | 0.039 | 0.045 | 0.51 | -0.024 | | |
| $I_2 \& T_b(H,V,40^\circ-45^\circ),T$ | 0.85 | 0.056 | 0.036 | 0.043 | 0.49 | -0.025 | 0.86 | 0.71 |
| $I_2 \& T_b(H,V,40^\circ-45^\circ),VI$ | 0.85 | 0.057 | 0.037 | 0.038 | 0.54 | -0.024 | | |
| $I_2 \& T_b(H,V,40^\circ-45^\circ),VI,T$ | 0.87 | 0.054 | 0.034 | 0.039 | 0.50 | -0.024 | 0.87 | 0.74 |
| $I_2 \& T_b(H,V,35^\circ-45^\circ)$ | 0.86 | 0.055 | 0.036 | 0.048 | 0.52 | -0.021 | | |
| $I_2 \& T_b(H,V,35^\circ-45^\circ),T$ | 0.89 | 0.050 | 0.031 | 0.045 | 0.51 | -0.022 | 0.87 | 0.72 |
| $I_2 \& T_b(H,V,35^\circ-45^\circ),VI$ | 0.88 | 0.052 | 0.033 | 0.042 | 0.54 | -0.022 | | |
| $I_2 \& T_b(H,V,35^\circ-45^\circ),VI,T$ | 0.89 | 0.048 | 0.030 | 0.042 | 0.52 | -0.021 | 0.88 | 0.74 |
| $I_2 \& T_b(H,V,30^\circ-45^\circ)$ | 0.89 | 0.048 | 0.032 | 0.051 | 0.54 | -0.023 | | |
| $I_2 \& T_b(H,V,30^\circ-45^\circ),T$ | 0.92 | 0.043 | 0.027 | 0.049 | 0.55 | -0.024 | 0.89 | 0.79 |
| $I_2 \& T_b(H,V,30^\circ-45^\circ),VI$ | 0.90 | 0.047 | 0.030 | 0.046 | 0.56 | -0.022 | | |
| $I_2 \& T_b(H,V,30^\circ-45^\circ),VI,T$ | 0.92 | 0.042 | 0.026 | 0.047 | 0.55 | -0.022 | 0.91 | 0.79 |
| $I_2 \& T_b(H,V,25^\circ-45^\circ)$ | 0.91 | 0.044 | 0.029 | 0.052 | 0.55 | -0.027 | | |
| $I_2 \& T_b(H,V,25^\circ-45^\circ),T$ | 0.93 | 0.038 | 0.023 | 0.050 | 0.55 | -0.028 | | |
| $I_2 \& T_b(H,V,25^\circ-45^\circ),VI$ | 0.92 | 0.042 | 0.027 | 0.047 | 0.58 | -0.030 | | |
| $I_2 \& T_b(H,V,25^\circ-45^\circ),VI,T$ | 0.94 | 0.037 | 0.023 | 0.048 | 0.56 | -0.029 | | |
| $I_2 \& T_b(H,V,25^\circ-60^\circ),VI$ | 0.93 | 0.037 | 0.024 | 0.047 | 0.56 | -0.033 | | |
| $I_2 \& T_b(H,V,25^\circ-60^\circ),T$ | 0.95 | 0.033 | 0.021 | 0.046 | 0.54 | -0.031 | | |
| $I_2 \& T_b(H,V,25^\circ-60^\circ),VI,T$ | 0.95 | 0.032 | 0.020 | 0.048 | 0.55 | -0.033 | 0.92 | 0.83 |

It is interesting to note that the performance of the NN retrieval [$I_2 \& T_b(30^\circ-45^\circ), T$] with respect to *in situ* data (columns 5-7 of Table 2) are actually better than those of the operational SMOS

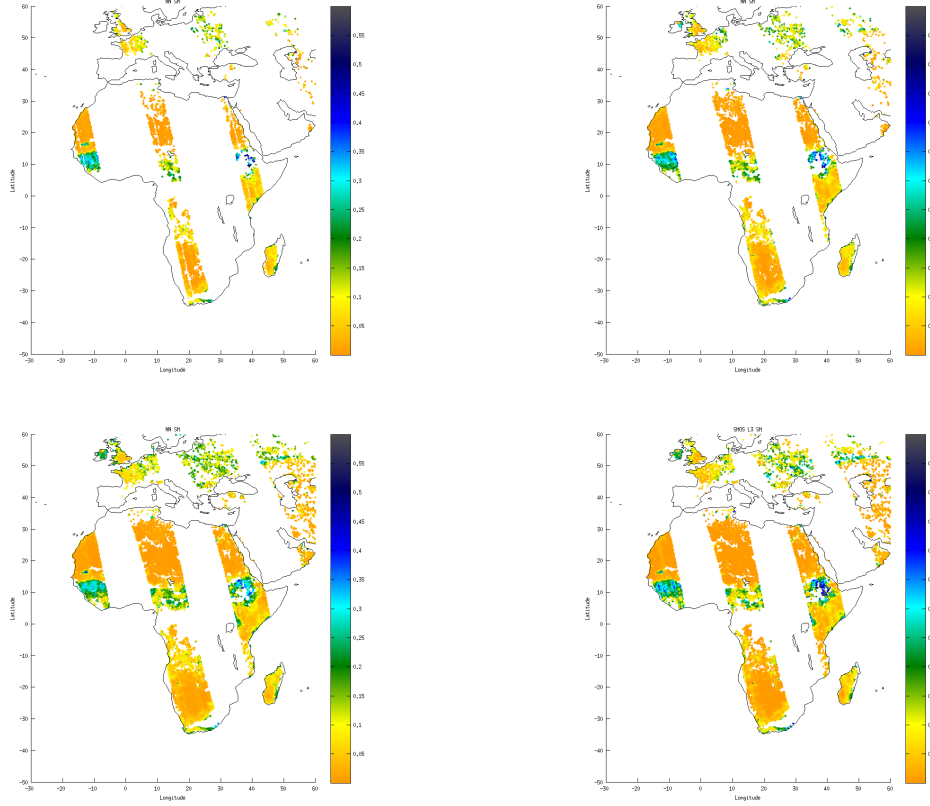


Figure 1: Soil moisture retrievals from NNs : $[I_2&T_b/(H,V,25^\circ-60^\circ),VI,T]$ (upper left), $[I_2&T_b(H,V,30^\circ-45^\circ),VI,T]$ (upper right) and $[I_2&T_b(H,V,40^\circ-45^\circ),VI,T]$ (bottom left) for day 1-8-2011. The bottom right is the SMOS L3 SM map for the same day. All the data correspond to SMOS ascending orbits.

L3 SM, and close to those of ECMWF SM_{0-7cm} (Table 1).

Figure 2 show the maps of temporal correlation with SMOS L3 SM for different NN retrievals. The main differences arise in high northern latitudes, where R_{temp} increases for the NN retrievals that show a higher mean R_{temp} in Table 2.

2.2 Sensitivity to the probability of RFI

The R_{temp} values discussed in the previous sections have been computed after inversion of 3 years times series of NN SM for all grid points without taking into account the RFI probability as given in the SMOS SM product. It is pertinent to understand how a RFI probability threshold would change the values presented in Table 2. Figure 3 and Table 3 show some maps and global statistics of the temporal correlation of NN SM and SMOS L3 SM for NN $[I_1 \& T_b$'s (H,V, $30^\circ-45^\circ$), T, tex] and for different upper limits of the RFI probability. Some, but not all, of the globe regions with the lowest R_{temp} are actually regions with RFI probability higher than 10 %. Therefore, as expected the mean R_{temp} value over the globe increases as the RFI probability threshold decreases. Whether the NN SM is an improvement with respect to SMOS L3 SM in those regions of higher RFI

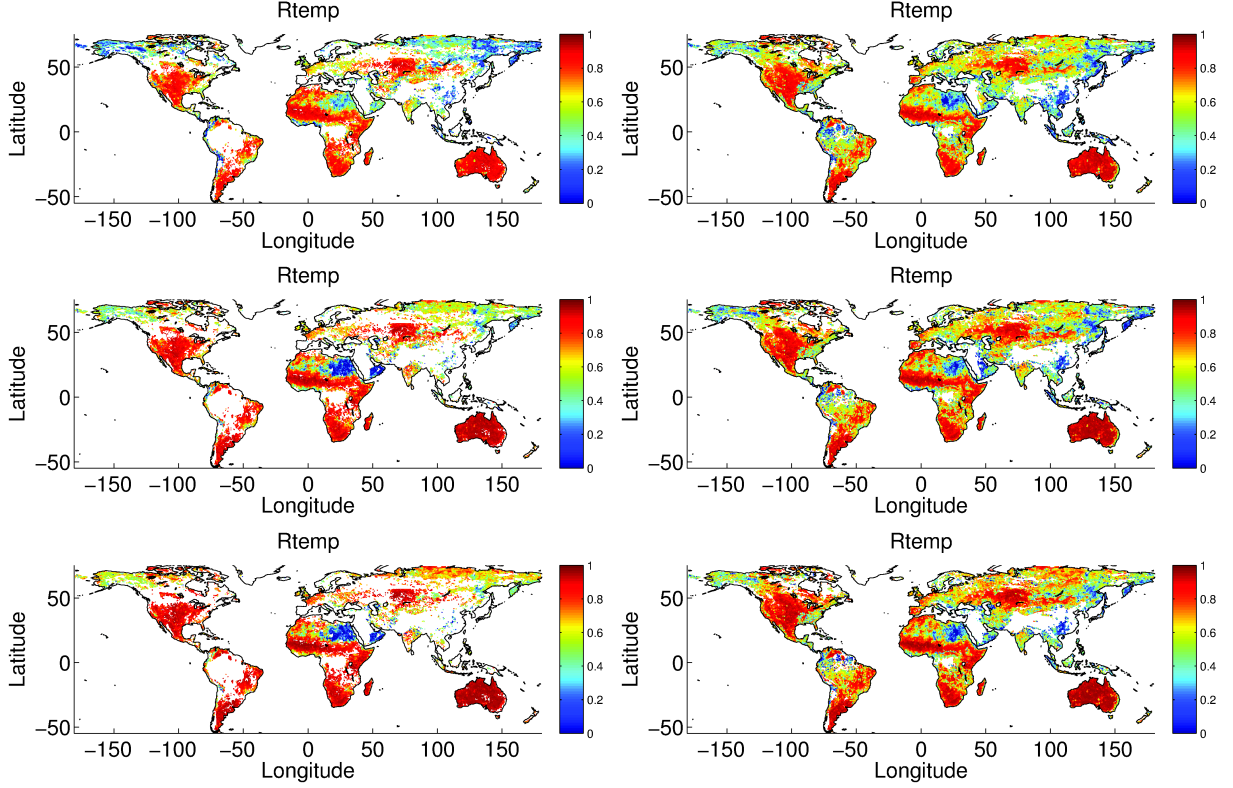


Figure 2: Temporal correlation for all grid points for NNs. Left panels, from top to bottom: $[I_2&T_b(H, V, 35^\circ-45^\circ), T, NDVI]$, $[I_2&T_b(H, V, 30^\circ-45^\circ), T, NDVI]$, $[I_2&T_b(H, V, 25^\circ-60^\circ), T, NDVI]$, Right panels, from top to bottom $[I_1&T_b(H, V, 30^\circ-45^\circ), T]$, $[I_1&T_b(H, V, 30^\circ-45^\circ), T, NDVI]$, $[I_1&T_b(H, V, 25^\circ-60^\circ), T]$.

Table 3: Mean R_{temp} of the SM produced with NN $[I_1&6T_b(30^\circ-45^\circ), T, tex]$ and SMOS L3 SM as a function of a RFI probability threshold

| RFI Prob upper limit | Mean R_{temp} |
|----------------------|-----------------|
| 100 | 0.74 |
| 20 | 0.76 |
| 15 | 0.77 |
| 10 | 0.78 |

probability and low R_{temp} would need further investigation. In any case, it is noteworthy that regions of low R_{temp} and low RFI probability still exist at northern latitudes.

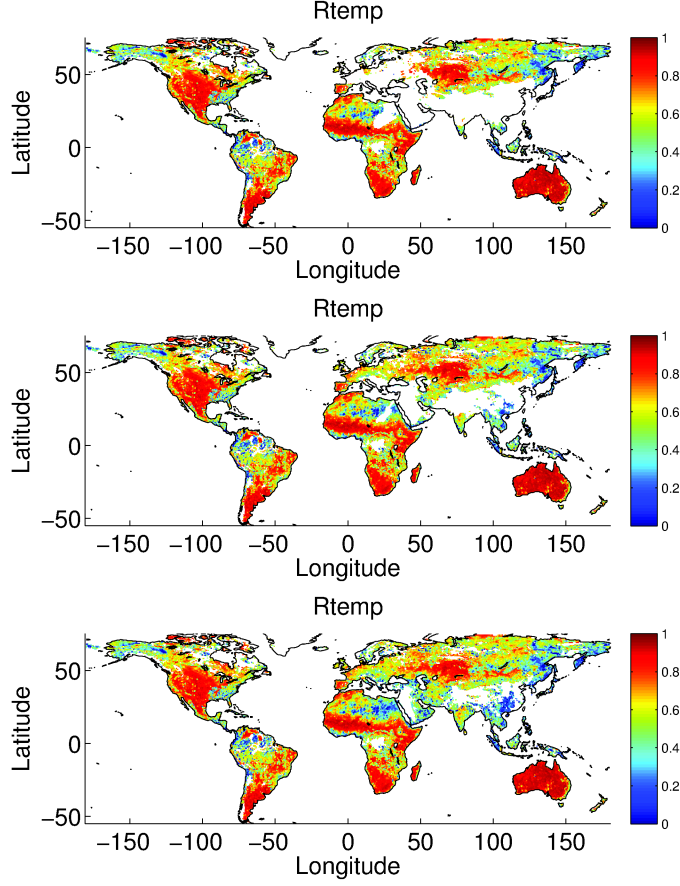


Figure 3: Temporal correlation for all grid points for NN [I_1 & $T_b(30^\circ-45^\circ)$, T, tex] and for an RFI probability lower than 10%, 20% or 100% (from top to bottom).

2.3 Computation of T_b 's and SM local extremes tables

The effect of residual low level RFI in the computation of normalized indexes I_2 has been studied. RFI can affect significantly T_b^{max} in some regions (Figure 4 shows an example in Northern Africa, Europe and the Middle Est). The upper-right panel of Figure 4 shows that it is possible to improve the computation of the T_b^{max} values requiring a valid SMOS L3 retrieval for the point and the time of the T_b^{max} acquisition.

In addition, requiring the existence of a valid SM value associated to the T_b guarantees the possibility of computing index I_2 . Therefore more retrievals can be obtained (compare left and right middle panels of Figure 4).

An additional constrain to compute I_2 will be to compute T_b 's percentiles and filter out the highest 10 % T_b 's, for instance, to compute I_2 . Nevertheless, it is worth noting that even if the input T_b 's is unrealistic, using this T_b with the associated SM value computed with the operational algorithm will also be used by the NN as an additional constrain to invert the forward model.

Table 4 shows the NN SM performance with respect to L3 SM at global scale and Table 5 shows the evaluation against the same *in situ* sites used for Table 2. When a L3SM value is required to update the min/max tables

Table 4: Performances of the non-linear regression (NN SM vs L3 SM) before and after requiring L3SM.

| neurons | orbit | R | RMSE | MAE |
|-----------------|-------|------|-------|-------|
| without L3SM | | | | |
| 5 | A | 0.91 | 0.044 | 0.028 |
| 7 | A | 0.91 | 0.044 | 0.028 |
| 7 | D | 0.91 | 0.048 | 0.032 |
| requiering L3SM | | | | |
| 5 | A | 0.89 | 0.046 | 0.029 |
| 7 | A | 0.90 | 0.045 | 0.028 |
| 7 | D | 0.90 | 0.048 | 0.031 |

Table 5: Performances with respect to *in situ* measurements before and after requiring L3SM.

| orbit | neurons | $\langle STD \rangle$ | R | Bias |
|-----------------|---------|-----------------------|------|--------|
| without L3SM | | | | |
| A | 5 | 0.048 | 0.55 | -0.022 |
| A | 7 | 0.049 | 0.54 | -0.023 |
| D | 7 | 0.051 | 0.53 | -0.035 |
| requiering L3SM | | | | |
| A | 5 | 0.047 | 0.54 | -0.028 |
| A | 7 | 0.048 | 0.54 | -0.029 |
| D | 7 | 0.051 | 0.48 | -0.032 |

the global performances of the NN SM both with respect to L3SM globally and with respect to *in situ* sites decrease slightly. The reason is that in this case one gets more retrievals using I_2 , but actually those grid points are points with significant RFI probability, which make the global performances decrease.

2.4 Number of neurons

The effect of the number of neurons in the hidden layer has been evaluated by computing both the global performances with respect to L3 SM (Table 6) and with respect to *in situ* measurements (Table 7).

The performances improve up to 4-5 neurons and remain constant for more neurons. **Therefore, for the shake of simplicity, the recommended architecture for the NRT processor is 5 neurons in the hidden layer** (and one neuron in the second or output layer).

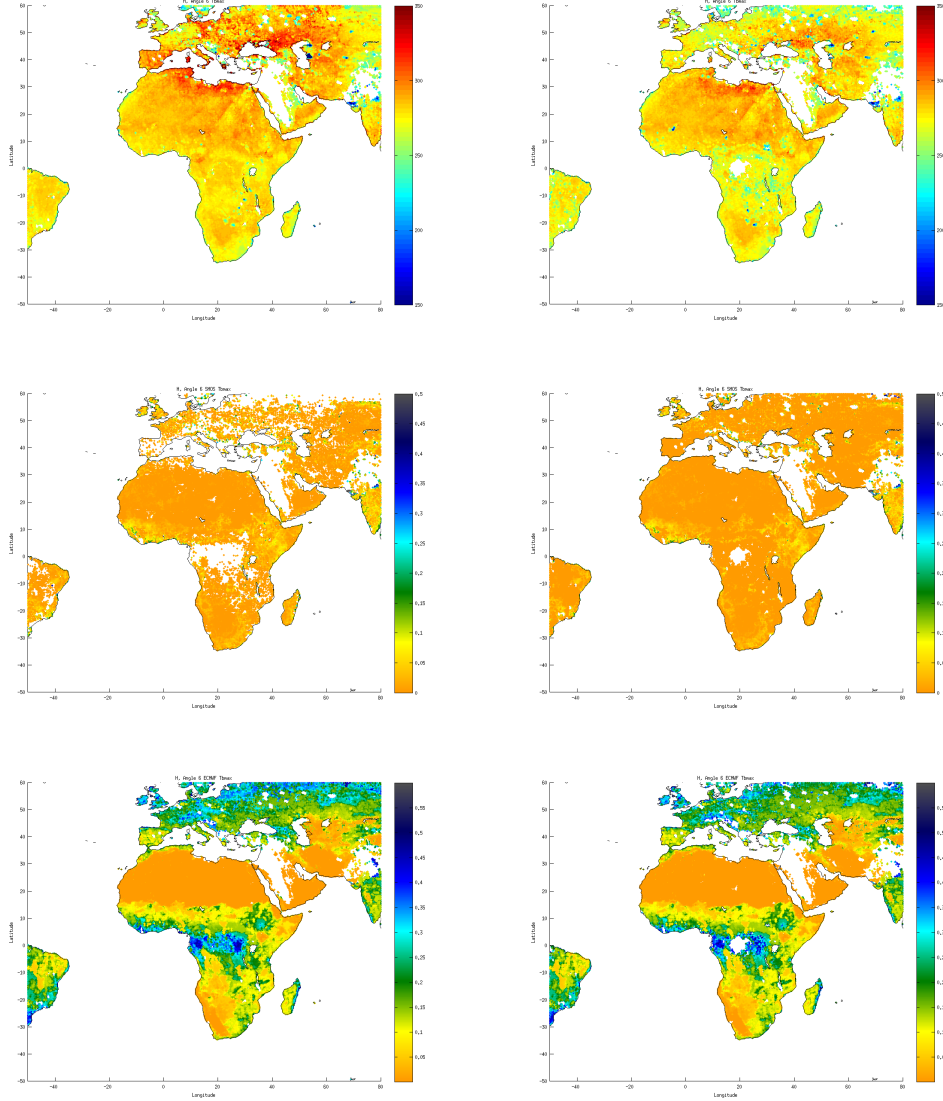


Figure 4: **Upper row, T_b^{max}** : left no L3 SM constrain. Right: requiring an L3 SM retrieval to update the max-min table. Otherwise, a given high T_b is discarded. **Middle row, L3 SM associated to T_b^{max}** : left no L3 SM constrain. Right: requiring an L3 SM retrieval to update the max-min table. Otherwise, a given high T_b is discarded. **Lower row, ECMWF layer 1 SM associated to T_b^{max}** : left no L3 SM constrain. Right: requiring an L3 SM retrieval to update the max-min table. Otherwise, a given high T_b is discarded.

Table 6: Performances of the non-linear regression (NN SM vs L3 SM) for different number of neurons in the hidden layer

| neurons | orbit | R | RMSE | MAE |
|---------|-------|-------|-------|-------|
| 1 | A | 0.890 | 0.049 | 0.032 |
| 2 | A | 0.910 | 0.045 | 0.029 |
| 3 | A | 0.900 | 0.046 | 0.030 |
| 4 | A | 0.910 | 0.044 | 0.028 |
| 5 | A | 0.910 | 0.044 | 0.028 |
| 6 | A | 0.910 | 0.044 | 0.028 |
| 7 | A | 0.910 | 0.044 | 0.028 |
| 8 | A | 0.910 | 0.045 | 0.028 |
| 10 | A | 0.910 | 0.044 | 0.028 |
| 6 | D | 0.910 | 0.048 | 0.031 |
| 7 | D | 0.910 | 0.048 | 0.032 |
| 8 | D | 0.910 | 0.048 | 0.032 |

Table 7: Performances with respect to *in situ* measurements for different number of neurons in the hidden layer (“NN-nX” means NN with X neurons in the hidden layer). For comparison the statistics obtained by comparing ECMWF SM and SMOS L3 SM with respect to the *in situ* sites are also shown in the table.

| orbit | SM | STD | R | Bias |
|-------|--------|-------|------|--------|
| A | NN-n1 | 0.047 | 0.53 | -0.021 |
| A | NN-n2 | 0.048 | 0.55 | -0.023 |
| A | NN-n3 | 0.047 | 0.55 | -0.021 |
| A | NN-n4 | 0.048 | 0.54 | -0.022 |
| A | NN-n5 | 0.048 | 0.55 | -0.022 |
| A | NN-n6 | 0.048 | 0.54 | -0.023 |
| A | NN-n7 | 0.049 | 0.54 | -0.023 |
| A | NN-n8 | 0.048 | 0.54 | -0.023 |
| A | NN-n10 | 0.048 | 0.54 | -0.024 |
| A | ECMWF | 0.047 | 0.57 | 0.050 |
| A | L3SM | 0.062 | 0.51 | -0.018 |
| D | NN-n6 | 0.051 | 0.53 | -0.036 |
| D | NN-n7 | 0.051 | 0.53 | -0.035 |
| D | NN-n8 | 0.051 | 0.52 | -0.035 |
| D | ECMWF | 0.056 | 0.58 | 0.056 |
| D | L3 SM | 0.065 | 0.48 | -0.027 |

3 Evaluation of the recommended NN configuration for the NRT SM processor

This section presents further evaluation of the SM dataset produced with the recommended configuration for the NRT SM processor, namely, using SMOS T_b 's from 30° to 45° incidence angles in 5° bins for both H and V polarizations, the corresponding I_2 normalized indexes, and the 0-7 cm soil temperature forecast by ECMWF. The NN architecture is two layers with a hidden layer containing 5 neurons.

A new training data base have been computed using one day every ten over the three years period and one grid point over three both in latitude and longitude. The maximum and minimum T_b 's tables (per incidence angle and polarization) have been updated only if a L3 SM value is available at the time of the T_b maximum.

3.1 Comparison to SMOS L3 SM

Figures 5 and 6 show the maps of temporal correlation of the NRT SM prototype with respect to the reference SMOS L3 SM both for ascending and descending orbits. The correlation of both products is very high (> 0.8) for all grid points except at high latitudes. The correlation at the Sahara desert is lower than the average, in particular for descending orbits. Lower correlation in this region of low SM values is expected because the

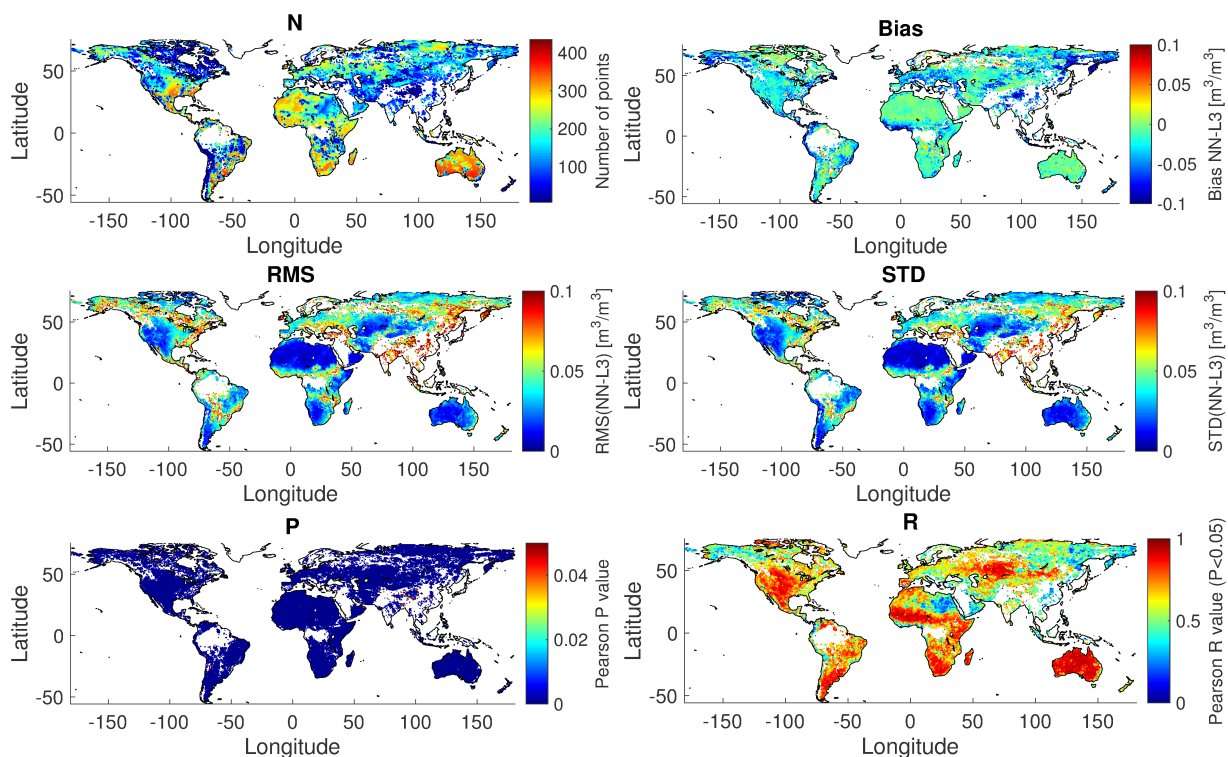


Figure 5: Comparison of SMOS L3 SM and the NN SM computed with the proposed configuration for the NRT product (angles from 30° to 45° plus soil temperature, one hidden layer with 5 neurons). N: number of points in the local time series. Bias: mean NN SM minus mean L3 SM. RMS: root mean square of the difference time series (NN SM - L3 SM). STD: standard deviation of the different time series. R: Pearson correlation coefficient. P: probability that the corresponding R value has been obtained by chance.

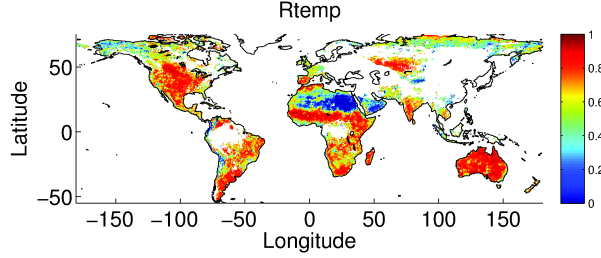


Figure 6: Same as the right-bottom panel of Fig. 5 but for descending orbits.

relative error of SM is higher than in regions of higher SM values. Actually, Figure 5 also shows that the RMS of the difference of L3 SM with respect of NN SM is also very low in this region. In addition, the eastern Sahara can be affected by RFI sources in the Middle-East region. Further discussion can be found in Mecklenburg et al. (2016).

The NRT SM retrieval will be done orbit per orbit, however, to get further insight into the comparison of the NRT-prototype SM and L3 SM it is interesting to average the data over a larger period. Figure 7 shows a monthly average for July 2012 of SMOS L3 SM and the NRT SM. Both maps contains the same spatial structures. The difference map, also in Fig. 7, shows some underestimation of NRT SM with respect to L3 SM in regions of high SM values such as the tropical regions. The lower-right panel of Fig. 7 shows the standard deviation, the root-mean-squared error and the bias of the NRT SM with respect to L3 SM averaged in bins of SM. From 0 to $0.25 \text{ m}^3/\text{m}^3$ the average negative bias of NRT SM is lower than $0.02 \text{ m}^3/\text{m}^3$ while for the highest SM values (less well represented in the training data base) to negative bias can increase up to $0.04\text{-}0.05 \text{ m}^3/\text{m}^3$.

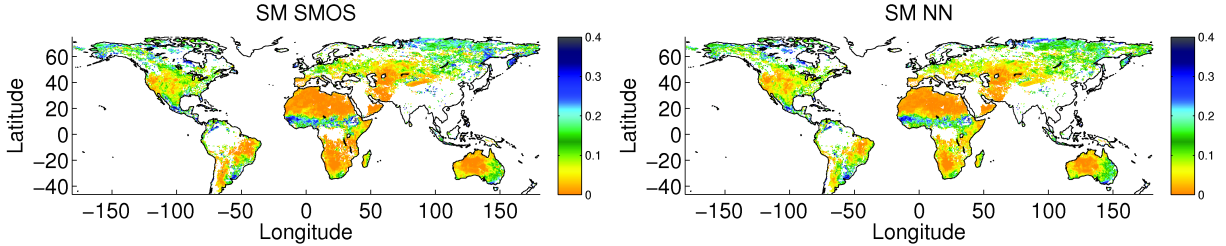


Figure 7: Comparison of the average SM computed for July 2012 using SMOS L3 SM (left) and NN SM (right) using the proposed configuration for the NRT product (angles from 30° to 45° plus soil temperature, one hidden layer with 5 neurons). Both maps correspond to ascending orbits.

3.2 Comparison to in situ measurements

The output of the proposed NRT NN configuration ($[6I_2, 6T_b, T]$ and 5 neurons in the hidden layer) has been further evaluated against a large number of *in situ* measurements retrieved from the International Soil Moisture Network (Dorigo et al., 2011). In addition, the SMOS L3 SM product and ECMWF IFS SM (0-7 cm) have also been evaluated against those measurements. For each in situ measurement, the closest CATDS grid point is selected. For this point the NRT SM, L3 SM and ECMWF SM are compared to the *in situ* measurement. The standard deviation, the Pearson correlation and the bias are computed using only times for which a SM value

is available for the four datasets. Finally, the mean of those values over a given network of sensors is computed. Table 8 shows the results.

The values obtained for the NRT SM are comparable but somewhat better than those obtained with the L3 SM. For instance, the mean correlation with respect to in situ data is 15 % higher and the mean STD is lower by up to $0.02 \text{ m}^3/\text{m}^3$ than those of SMOS L3 for some networks such as AMMA. The only two networks where SMOS L3 SM give slightly higher correlation with in situ data are OzNet for the 0-5 cm depth sensors and HOBE.

More detailed evaluation against *in situ* measurements analyzed as a function of vegetation parameters, topography or roughness can be found in Kerr et al. (2016).

Table 8: Evaluation of the proposed NN, ECMWF IFS (0-7 cm) and SMOS L3 SM against *in situ* measurements. NRT SM has been obtained using (6I2,6Tbs,T) as input and 5 neurons in the hidden layer. For each network, the table give the STD, Pearson R and Bias averaged across all the network sites taken into account (number of sites is given as "Sensors" and the average number of points in the time series is given as N_p). The upper and lower depth of the sensors is given in meters, following the network name.

| SM | STD | R | Bias | STD | R | Bias |
|---------|-------|-------|--------------------------|-----------|-------|-------------------------------------|
| AMMA | 0.05 | 0.05 | Sensors: 6; $N_p = 53$ | SMOSMANIA | 0.05 | 0.05 : Sensors: 13; $< N_p \geq 62$ |
| NRT | 0.061 | 0.566 | 0.009 | 0.047 | 0.613 | -0.132 |
| ECMWF | 0.027 | 0.601 | 0.044 | 0.074 | 0.792 | 0.085 |
| SMOS L3 | 0.069 | 0.476 | 0.003 | 0.069 | 0.611 | -0.107 |
| ARM | 0.025 | 0.025 | Sites 9; $N_p = 124$ | SCAN | 0.05 | 0.05 : Sensors: 106; $N_p = 100$ |
| NRT | 0.064 | 0.750 | -0.062 | 0.048 | 0.533 | -0.030 |
| ECMWF | 0.074 | 0.715 | 0.078 | 0.059 | 0.525 | 0.058 |
| SMOS L3 | 0.084 | 0.679 | -0.045 | 0.063 | 0.504 | -0.023 |
| RM | 0.05 | 0.05 | Sensors: 16; $N_p = 128$ | SNOTEL | 0.05 | 0.05 : Sensors: 173; $N_p = 82$ |
| NRT | 0.068 | 0.676 | -0.158 | 0.041 | 0.454 | -0.065 |
| ECMWF | 0.074 | 0.615 | -0.051 | 0.045 | 0.471 | 0.040 |
| SMOS L3 | 0.082 | 0.603 | -0.143 | 0.058 | 0.391 | -0.054 |
| HOBE | 0.00 | 0.05 | Sensors: 42; $N_p = 58$ | UDC-SMOS | 0.00 | 0.10 : Sensors: 1; $N_p = 34$ |
| NRT | 0.053 | 0.470 | -0.083 | 0.045 | 0.336 | -0.266 |
| ECMWF | 0.044 | 0.617 | 0.026 | 0.025 | 0.529 | -0.051 |
| SMOS L3 | 0.075 | 0.500 | -0.107 | 0.077 | 0.275 | -0.196 |
| OZNET | 0.00 | 0.05 | Sites 8; $N_p = 36$ | UDC-SMOS | 0.05 | 0.05 : Sensors: 4 $N_p = 32$ |
| NRT | 0.080 | 0.734 | -0.022 | 0.046 | 0.301 | -0.241 |
| ECMWF | 0.054 | 0.638 | 0.073 | 0.025 | 0.289 | -0.027 |
| SMOS L3 | 0.082 | 0.756 | -0.051 | 0.078 | 0.297 | -0.171 |
| OZNET | 0.00 | 0.08 | Sensors: 6; $N_p = 43$ | USCRN | 0.05 | 0.05 : Sensors: 53; $N_p = 115$ |
| NRT | 0.074 | 0.706 | -0.016 | 0.053 | 0.603 | -0.032 |
| ECMWF | 0.061 | 0.595 | 0.107 | 0.057 | 0.629 | 0.060 |
| SMOS L3 | 0.082 | 0.611 | 0.001 | 0.066 | 0.549 | -0.026 |
| PBO-H2O | 0.00 | 0.05 | Sensors: 6; $N_p = 111$ | REMEDHUS | 0.00 | 0.05 : Sensors: 4 $N_p = 173$ |
| NRT | 0.048 | 0.718 | -0.063 | 0.052 | 0.696 | 0.014 |
| ECMWF | 0.049 | 0.615 | 0.057 | 0.098 | 0.665 | 0.173 |
| SMOS L3 | 0.059 | 0.616 | -0.057 | 0.063 | 0.682 | 0.026 |

4 The NRT SM processor implementation

4.1 Global architecture

The structure of the NRT SM processor is shown in the flow chart depicted in Figure 8. The processor can be divided in three preprocessing blocks and the actual NRT SM processor containing the implementation of the NN.

ECMWF processor The first preprocessing block will extract information from ECMWF IFS such as snow depth soil temperature to filter out frozen soil or soil covered by snow. The soil temperature will also be used as input to the NN.

SMOS T_b 's processor The second preprocessing block is devoted to transform the NRT ECMWF SMOS T_b 's into a dataset similar to CATDS L3TB T_b 's (Berthon et al., 2013). The main steps consist in transform T_b 's in the antenna-based XY reference frame to the ground-based HV reference frame. A temporal interpolation of XY acquisitions should be done before to apply the rotation matrix to compute HV T_b 's as described by Quesney (2011). The second step will be to average the HV T_b 's in 5° incidence angle bins. Those operations should be applied to the NRT T_b 's that are distributed in BUFR format de Rosnay et al. (2012).

The off-line processor The third block is the off-line processor (grey box in Fig. 8), which is devoted to analyse the available time series of SMOS L2 SM to compute the SM values associated to the maximum and minimum T_b 's values for each polarization, incidence angle, and point of the ISEA grid. This is used to compute a maximum-minimum map that will be used to derive the local indexes I_1 and I_2 . In the context of the on-line NRT SM processor it will only be needed to update the maximum-minimum table if new extreme values are measured.

In addition, the off-line processor to construct a training and a test database containing all the input information needed by the NN and SMOS L2 SM. An off-line pre-processing of two years of SMOS data will be needed to train and test the NN and recompute weights and normalization parameters similar to those given in Tables 9, 10, 11 and 12, which have been computed using CATDS L3TB data.

Finally, the off-line processor has also been used to compute angle-binned T_b profiles in HV polarization from L1C data, in order to validate the output of the NRT T_b 's pre-processor.

NN NRT SM processor The core of the NRT SM processor is the NN processor, that will use the NN parameters to compute SM from the dataset prepared by the pre-processors. The output will be in the ISEA grid in NetCDF format. The output data will be

- The ISEA grid point number
- Latitude
- Longitude
- Year
- Month
- Day
- Seconds from midnight (all times should be UT)
- NRT soil moisture

Table 9: Input vector elements and minimum and maximum values to be used to normalize the input vectors. The numbers in parenthesis in the second column is the center of the incidence angle bin in degrees.

| | Elem. | v^{min} | v^{max} |
|---------------|---------------|-----------|-----------|
| $i = 1$ | $I_2^H(32.5)$ | 0 | 1 |
| 2 | $I_2^H(37.5)$ | 0 | 1 |
| 3 | $I_2^H(42.5)$ | 0 | 1 |
| 4 | $I_2^V(32.5)$ | 0 | 1 |
| 5 | $I_2^V(37.5)$ | 0 | 1 |
| 6 | $I_2^V(42.5)$ | 0 | 1 |
| 7 | $T_b^H(32.5)$ | 114.4383 | 378.6492 |
| 8 | $T_b^H(37.5)$ | 79.84862 | 351.2497 |
| 9 | $T_b^H(42.5)$ | 110.9225 | 349.0707 |
| 10 | $T_b^V(32.5)$ | 128.9407 | 352.0065 |
| 11 | $T_b^V(37.5)$ | 95.24826 | 367.8640 |
| 12 | $T_b^V(42.5)$ | 136.2956 | 366.7104 |
| $n_{in} = 13$ | $T_{(0-7cm)}$ | 274.0004 | 329.0676 |

- Soil moisture uncertainty
- RFI probability

Name conventions : file name conventions should follow ESA guidelines similar to those of the currently operational L2 SM product.

4.2 NRT SM algorithm

The NN used in the previous section has two layers. The first layer contains $j = 1, \dots, n_{L1}$ nodes or neurons with an hyperbolic tangent as activation function. The second layer contains a single neuron with a linear function as activation function.

The number of elements in the input vector depends on the NN retrieval as discussed in Sect. 2. In the case of the recommended NN retrieval, using 6 T_b 's (H and V for incidence angle bins from 30 to 45°), 6 index I_2 (H and V for incidence angle bins from 30 to 45°), and ECMWF soil Temperature, the number of elements n_{in} is 13. The order of the $i = 1, \dots, n_{in}$ elements in the input vector should be preserved as the trained NN should be applied to an input vector v of the same characteristics than those used for the training. The order of the elements is given in the second column of Table 9.

The inputs range should be re-normalized to have values in the $[-1, 1]$ range. The each input vector element, the minimum and maximum values determined during the training phase are given by the vectors v_i^{min} and v_i^{max} ($i = 1, \dots, n_{in}$). The vector elements are given by Table 9.

$$v_i^{norm} = -1 + 2 \frac{v_i - v_i^{min}}{v_i^{max} - v_i^{min}}, \quad \forall i = 1 \dots n_{in} \quad (3)$$

The normalized input, together with the first layer weights (W_{L1}) and bias B_{L1} are used to compute the first layer outputs v^{L1} as follows:

$$v_j^{L1} = \tanh\left(\sum_{i=1}^{n_{in}} W_{L1}^{ij} v_i^{norm} + B_{L1}^j\right), \quad \forall j = 1 \dots n_{L1} \quad (4)$$

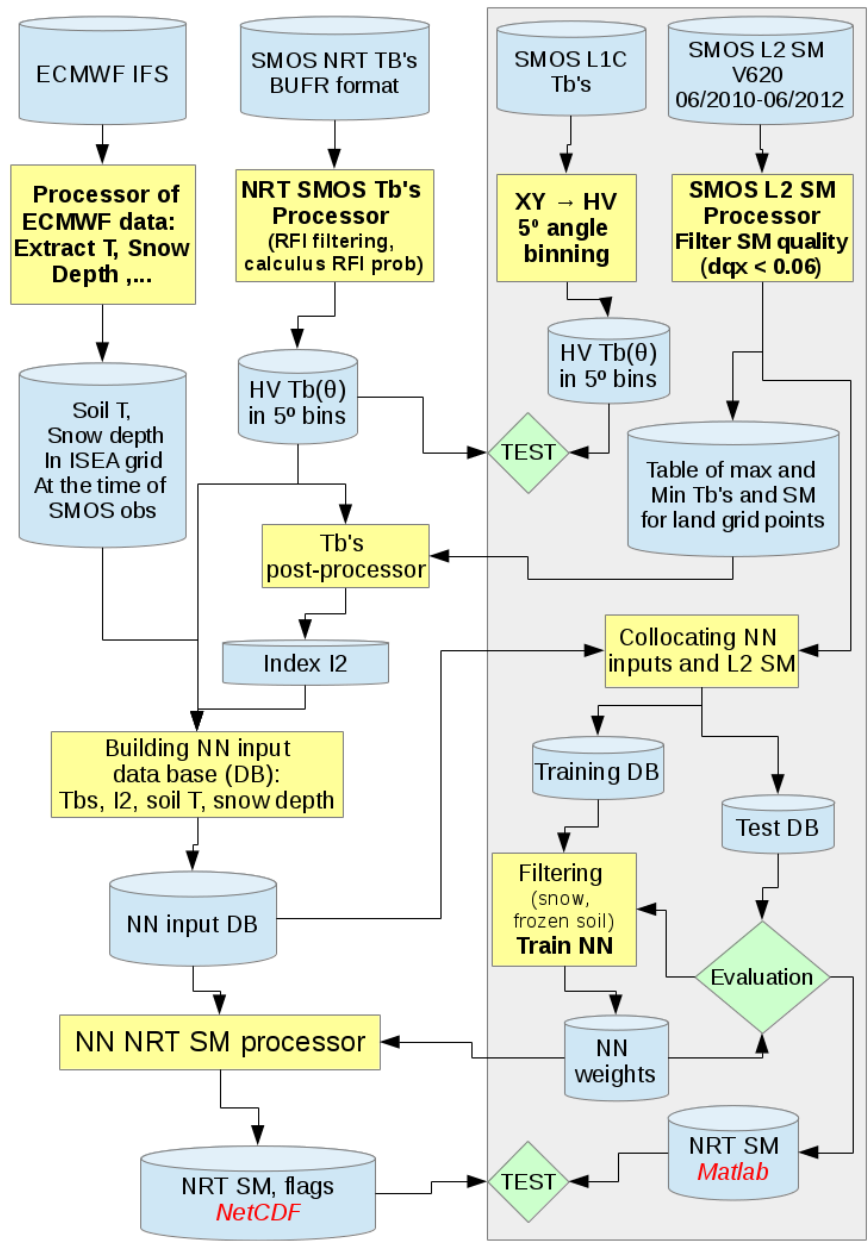


Figure 8: Flow chart of the NRT SM processor. The right-hand part, shown in a grey box, is the off-line processor (see Sect. 4).

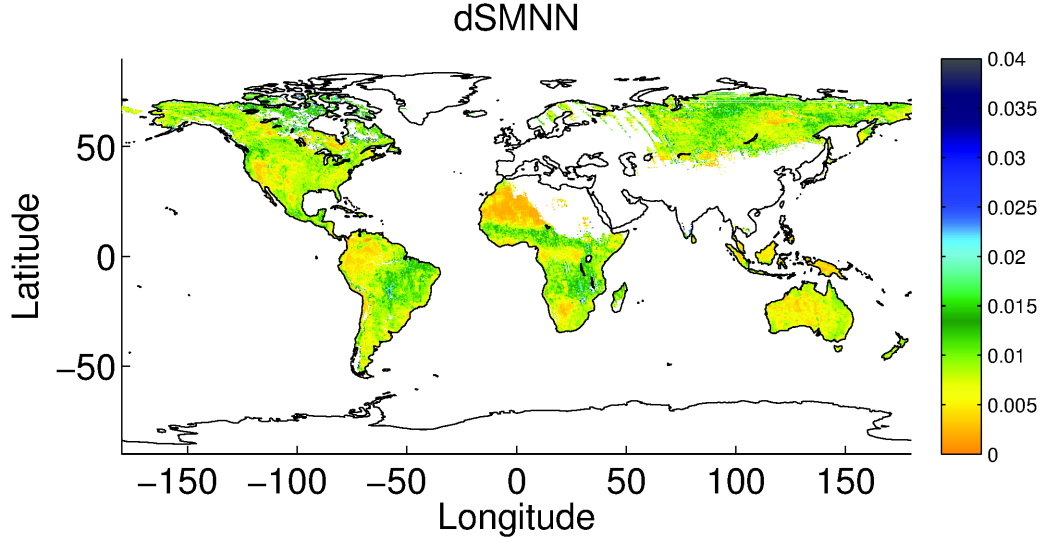


Figure 9: Example of the neural network output uncertainty taking into account the uncertainty in the inputs as described in Sect. 4.2.1. The figure shows the monthly mean for september 2012 of the output uncertainties of a neural network using as input T_b 's from 7 angles bins 25 to 60° for H and V polarizations and the associated indexes I_2 . In this example the reference SM used to train the NN were ECMWF simulated fields for which the associated uncertainty used to compute ΔI_2 is supposed to be $0.01 \text{ m}^3/\text{m}^3$.

The values of W_{L1} and bias B_{L1} for the selected NN retrieval are given in Tables 10 and 11, respectively. The output of the second layer is computed from the first layer outputs, and the second layer weights (W_{L2}) and bias B_{L2} as follows:

$$v^{L2} = \sum_{j=1}^{n_{L1}} W_{L2}^j v_j^{L1} + B_{L2} \quad (5)$$

The values of W_{L2} and bias B_{L2} for the selected NN retrieval are given in Table 11. Finally, to obtain the NN output (v^{out}), the output of the second layer has to be re-normalized as follows:

$$v^{out} = v_{newMin}^{L2} + \frac{v_{newMax}^{L2} - v_{newMin}^{L2}}{v_{oldMax}^{L2} - v_{oldMin}^{L2}} (v^{L2} - v_{oldMin}^{L2}); \quad (6)$$

Where v_{min}^{L2} and v_{max}^{L2} are given in Table 12

4.2.1 Neural network output uncertainties

From the definitions of $I_{2\lambda\phi}(t)$ and $I_{1\lambda\phi}(t)$ given by Eqs. 1 and 2, their associated uncertainties $\Delta I_{2\lambda\phi}(t)$ and $\Delta I_{1\lambda\phi}(t)$ can be computed from uncertainties in T_b 's, in the maximum and minimum T_b 's and the associated SM values as follows:

$$\Delta I_{2\lambda\phi}(t) = \left\{ [SM_{\lambda\phi}^{T_b^{max}} - SM_{\lambda\phi}^{T_b^{min}}]^2 (\Delta I_{1\lambda\phi}(t))^2 + [1 - I_{1\lambda\phi}(t)]^2 (\Delta SM_{\lambda\phi}^{T_b^{min}})^2 + [I_{1\lambda\phi}(t)]^2 (\Delta SM_{\lambda\phi}^{T_b^{max}})^2 \right\}^{1/2} \quad (7)$$

Table 10: Weights of the first layer of neurons (W^{L1}) for each vector element i and neuron j .

| | | | | | |
|--------------|----------|---------|---------------|---------|---------|
| | $i = 1$ | 2 | 3 | 4 | 5 |
| $j = 1$ | 0.0490 | 0.0378 | -0.0653 | 0.4429 | 0.6987 |
| 2 | -0.3376 | -0.4613 | -3.0195 | -1.0157 | 0.3622 |
| 3 | 0.2998 | 0.1886 | 0.3546 | 0.4974 | 0.4872 |
| 4 | 0.0855 | 0.1634 | 0.2540 | -0.0130 | -0.1111 |
| $n_{L1} = 5$ | -0.0081 | 0.0359 | 0.1098 | -0.1475 | -0.2626 |
| | $i = 7$ | $i = 8$ | 9 | 10 | 6 |
| $j = 1$ | -0.04461 | -0.1103 | 1.9651 | -1.0806 | 0.2529 |
| 2 | 5.02267 | -1.7251 | -1.6339 | -3.6595 | -0.1443 |
| 3 | -1.96481 | 0.6306 | 2.7054 | -4.3560 | 0.4335 |
| 4 | 1.53524 | -0.9316 | -3.2885 | 2.2879 | 0.1173 |
| $n_{L1} = 5$ | 1.44401 | -0.7325 | -3.2665 | 2.2129 | 0.0167 |
| | $i = 11$ | 12 | $n_{in} = 13$ | | |
| $j = 1$ | -0.4568 | 0.6786 | 0.1338 | | |
| 2 | -6.8144 | -0.0754 | 2.2320 | | |
| 3 | -2.6084 | -3.5778 | 1.3706 | | |
| 4 | 0.7711 | 0.9056 | -0.4459 | | |
| $n_{L1} = 5$ | 0.7070 | 0.6553 | -0.4459 | | |

Where $\Delta I_{1\lambda\phi}(t)$ is given by:

$$\Delta I_{1\lambda\phi}(t) = \frac{1}{T_{D\lambda\phi}} \left[\Delta T_{b\lambda\phi}(t)^2 + \left(\frac{T_{m\lambda\phi}(t)}{T_{D\lambda\phi}} \Delta T_{b\lambda\phi}^{max} \right)^2 + \left\{ \left(-1 + \frac{T_{m\lambda\phi}(t)}{T_{D\lambda\phi}} \right) \Delta T_{b\lambda\phi}^{min} \right\}^2 \right]^{1/2}, \quad (8)$$

$$(9)$$

as a function of the uncertainty of the local instantaneous measurement $\Delta T_{b\lambda\phi}(t)$ and the uncertainties of the local extreme T_b 's values ($\Delta T_{b\lambda\phi}^{max}$ and $\Delta T_{b\lambda\phi}^{min}$).

The uncertainties of the NN output given by Eqs. 3-6 can be estimated from the uncertainties in the input vector elements (Δv_i) as follows. First the uncertainties of the normalized input vector can be computed as:

$$\Delta v_i^{norm} = 2 \frac{\Delta v_i}{v_i^{max} - v_i^{min}}, \quad \forall i = 1 \dots n_{in} \quad (10)$$

Using those quantities, the uncertainty of the two layers neural network given by Eqs. 4 and 5 can be expressed as:

$$(\Delta v^{L2})^2 = \sum_{i=1}^{n_{in}} \left\{ (\Delta v_i^{norm})^2 \left(\sum_{j=1}^{n_{L1}} W_{L2}^j W_{L1}^{ij} \sigma^j \right)^2 \right\} \quad (11)$$

where σ^j is given by:

$$\sigma^j = 1 - \tanh^2 \left(\sum_{i=1}^{n_{in}} W_{L1}^{ij} v_i^{norm} + B_{L1}^j \right), \quad \forall j = 1 \dots n_{L1} \quad (12)$$

Finally, the uncertainty after the normalization of the output can be written as:

Table 11: Bias for the first layer of neurons (B^{L1}), weights for the second layer (W^{L2}), and bias for the second layer of neurons (B^{L2}).

| | B^{L1} | W^{L2} | B^{L2} |
|---------|----------|----------|----------|
| $j = 1$ | 0.168395 | -0.58412 | 1.1942 |
| 2 | 1.326084 | 0.030665 | ... |
| 3 | 3.479287 | 0.077504 | ... |
| 4 | 0.880560 | 2.193188 | ... |
| 5 | 0.243953 | -2.43620 | ... |

Table 12: Parameters ($v_{oldMax,newMin}^{L2}, \dots$) to apply to re-normalize the output of the NN (Eq. 6).

| | old | new |
|-----|-----|-----|
| Min | -1 | 0 |
| Max | 1 | 1 |

$$\Delta v^{out} = \frac{v_{newMax}^{L2} - v_{newMin}^{L2}}{v_{oldMax}^{L2} - v_{oldMin}^{L2}} \Delta v^{L2}, \quad (13)$$

Expressing the output uncertainty as Eq. 11 implies that the vector elements v_i are independent. However, when using index I_2 as input as well as the actual T_b 's, some elements are not independent. Since the uncertainties in Eq. 11 are expressed in quadratic form, Eq. 11 gives an upper limit to the output uncertainty. Figure 9 show an example of the output uncertainty for a NN using T_b 's and local indexes I_2 as inputs.

5 Summary

The best approach to retrieve soil moisture in Near-Real-Time (NRT) using networks has been discussed using SMOS CATDS Level 3 brightness temperatures and Level 3 soil moisture (SM). Neural network retrievals have been first evaluated comparing the output SM to the L3 SM used as reference during 2012. The global daily correlation (“spatial correlation”) and the local temporal correlations have also been computed and averaged in the June-2010 to June 2013 period. The NNs output has also been evaluated against in situ measurements over the SCAN network, the USDA ARS watersheds and OzNet.

The recommended input configuration is using SMOS T_b 's from 30° to 45° incidence angles in 5° bins for both H and V polarizations, the corresponding I_2 normalized indexes, and the 0-7 cm soil temperature forecast by ECMWF. The recommended NN architecture is two layers with a hidden layer containing 5 non-linear neurons and an output layer with one linear neuron. This configuration is the best trade-off of retrieved SM performance and retrieval swath width (914 km).

The recommended NN configuration for the NRT SM product has been specifically evaluated against the reference L3 SM data and against a large number of in situ measurements from the International Soil Moisture Network. Average statistics are somewhat better than those of the reference L3 SM data for most of the sites.

In summary, the recommended NN configuration performs as well or better than the reference SM dataset but the retrieval can be done in Near-Real-Time after a global training phase. Finally, the proposed global architecture of the NRT SM processor has been discussed and the NN algorithm has been described including the output uncertainty estimation.

References

- Berthon, L., et al., 2013: CATDS Level 3 data product description: Soil Moisture and Brightness Temperature part. *CESBIO report SO-TN-CB-CA-0001*, 1–38.
- de Rosnay, P., M. Dragosavac, M. Drusch, A. Gutiérrez, M. Rodríguez López, N. Wright, J. Muñoz Sabater, and C. R., 2012: SMOS NRT BUFR specification. SMOS-NRT-BUFR-ECMWF - v2.0, ECMWF.
- Dorigo, W., et al., 2011: The international soil moisture network: a data hosting facility for global in situ soil moisture measurements. *Hydrology and Earth System Sciences*, 15 (5), 1675–1698.
- Jackson, T. J., et al., 2012: Validation of soil moisture and ocean salinity (SMOS) soil moisture over watershed networks in the US. *Geoscience and Remote Sensing, IEEE Transactions on*, 50 (5), 1530–1543.
- Kerr, Y. H., et al., 2016: Overview of SMOS performances in term of global soil moisture monitoring after 5 years in operation. *Remote Sensing of Environment*, submitted.
- Mecklenburg, S., et al., 2016: ESA’s Soil Moisture and Ocean Salinity Mission: from science to operational applications. *Remote Sensing of Environment*, submitted.
- Quesney, A., 2011: Data Processing Model: traitements L3TB. Tech. Rep. CAT-DPM-CTL3TB-00061-CG, CapGemini Sud / ACRI-ST.
- Rodríguez-Fernández, N. J., P. Richaume, F. Aires, C. Prigent, J. Kerr, Y. H. Kolassa, C. Jiménez, F. Cabot, and A. Mahmoodi, 2013: Soil moisture retrieval from SMOS observations using neural networks. Tech. Rep. SMOS Ground Segment SO-TN-CB-GS-038, CESBIO, Toulouse, France.
- Rodríguez-Fernández, N. J., P. Richaume, Y. H. Kerr, F. Aires, C. Prigent, C. Jiménez, and A. Mahmoodi, 2014: Retrieving soil moisture from SMOS brightness temperatures by neural networks trained with simulated data. Tech. Rep. SMOS Ground Segment SO-TN-CB-GS-041, CESBIO, Toulouse, France.
- Rodríguez-Fernández, N. J., et al., 2015: Soil moisture retrieval using neural networks: application to SMOS. *IEEE Transactions on Geoscience and Remote Sensing*, Volume:PP , Issue: 99.
- Schaefer, G. L., M. H. Cosh, and T. J. Jackson, 2007: The USDA natural resources conservation service soil climate analysis network (SCAN). *Journal of Atmospheric and Oceanic Technology*, 24 (12), 2073–2077.
- Smith, A. B., et al., 2012: The murrumbidgee soil moisture monitoring network data set. *Water Resour. Res.*, 48.